

Ph.D. Thesis

**Probing Electroweakly Interacting
Massive Particles
with Drell-Yan Process
at 100 TeV Colliders**

So Chigusa

Department of Physics



THE UNIVERSITY OF TOKYO

December 2019

Abstract

(♣ To be written ♣)

Acknowledgments

(♣ To be written ♣)

Contents

| | | |
|----------|---|-----------|
| 1 | Introduction | 1 |
| 2 | Weakly interacting massive particles | 1 |
| 2.1 | WIMPs as a dark matter candidate | 1 |
| 2.2 | Brief review of models | 5 |
| 2.3 | WIMP DM search : indirect detection | 6 |
| 3 | Probing EWIMPs with Drell-Yan process at 100 TeV colliders | 7 |
| 3.1 | EWIMP effect on the lepton production processes | 7 |
| 3.2 | Analysis | 11 |
| 3.2.1 | Event generation | 11 |
| 3.2.2 | Statistical treatment | 12 |
| 3.2.3 | Detection reach | 16 |
| 3.2.4 | Determination of EWIMP properties | 18 |
| 3.3 | Conclusion | 22 |
| | Appendix A Review of supersymmetry | 24 |

Section 1

Introduction

- (♣ Unit: $\hbar = c = k_B = 1$ ♣)
- (♣ Convention: dot as time derivative ♣)
- (♣ Definition of “SM” ♣)
- (♣ Definition of “WIMP” ♣)

Section 2

Weakly interacting massive particles

2.1 WIMPs as a dark matter candidate

One of the most important evidences of the beyond SM is the existence of dark matter (DM) [1]. DM is an unknown object that occupies a non-negligible ratio of the total energy of our universe, but has not yet been directly observed because of its weak interaction with the SM particles.^{‡1} In spite of its invisibility, the existence of DM is confirmed by several astrophysical observations such as the mass measurement using the gravitational lensing effect caused by galaxies and clusters [2, 3], the flatness of galactic rotation curves further the optical radius [4, 5], the measurement of the power spectrum of the cosmic microwave background (CMB), and so on. In particular, the observation of CMB allows us the precise determination of various cosmological parameters [6, 7] including the density of the non-relativistic matter and baryon, which is currently determined as [8]

$$\Omega_m h^2 = 0.1430 \pm 0.0011, \quad (2.1)$$

$$\Omega_b h^2 = 0.02237 \pm 0.00015, \quad (2.2)$$

where $h \sim \mathcal{O}(1)$ is the Hubble constant in units of $100 \text{ km s}^{-1} \text{ Mpc}^{-1}$. The difference between $\Omega_m h^2$ and $\Omega_b h^2$ implies the existence of DM and its abundance $\Omega_\chi h^2 \simeq 0.12$.

In cosmology, DM production mechanisms that try to explain the DM abundance are divided into two main categories: thermal and non-thermal production. The former assumes the equilibrium between the DM and the thermal bath in the early universe. As the universe expands, the interaction rate that maintains the thermal equilibrium becomes smaller and

^{‡1}At worst DM interacts with the SM particles through the gravity, which is considerably weaker than all the other known interactions. (♣ Mention to Ema paper?? ♣)

the DM decouples from the thermal bath at some time, which is the so-called *freezeout*. As we will see below, the resulting abundance of the DM in this scenario is mainly controlled by the temperature of the thermal bath T_f when the freezeout occurs. On the other hand, non-thermal production assumes the DM production by some processes irrespective of the thermal bath such as decay of a heavy particle. Since the thermal production scenario can be realized in relatively simple setup and WIMPs are well motivated in connection with this kind of scenario, we focus on it.

We assume the stable DM particle χ with mass m_χ can pair annihilate into SM particles with some cross section σ . When DM is in thermal equilibrium with the thermal bath of temperature T , DM velocity obeys the corresponding Boltzmann distribution. Let v be the relative velocity of annihilating DM particles and $\langle\sigma v\rangle$ be the thermal average of the product of σ and v . By using this quantity, we can write down the Boltzmann equation for the DM number density n_χ as

$$\frac{d(n_\chi a^3)}{dt} = -a^3 \langle\sigma v\rangle (n_\chi^2 - n_{\text{eq}}^2), \quad (2.3)$$

where t and a are the time coordinate and the scale factor, respectively, of the Friedmann Robertson Walker metric

$$ds^2 = -dt^2 + a(t)^2 d\mathbf{x}^2, \quad (2.4)$$

while n_{eq} denotes the number density of DM in equilibrium. When DMs are non-relativistic, its temperature dependence is given by $n_{\text{eq}} \propto T^{3/2} \exp(-m_\chi/T)$. The first term of the right handed-side of Eq. (2.3) represents the annihilation rate of DM pairs that should be proportional to n_χ^2 , while the second term describes the DM creation through the inverse process. As desired, the number density does not change in time if $n_\chi = n_{\text{eq}}$. Recalling the total entropy conservation in a comoving volume $sa^3 = (\text{const})$, it turns out to be convenient to define the ratio $Y \equiv n_\chi/s$. In fact, this modification cancels the effect of the expansion of the universe $\dot{a} > 0$ from Eq. (2.3), leading to a simpler equation

$$\frac{dY}{dt} = -s \langle\sigma v\rangle (Y^2 - Y_{\text{eq}}^2), \quad (2.5)$$

with $Y_{\text{eq}} \equiv n_{\text{eq}}/s$.

Here we assume that the freezeout occurs when the relativistic radiation dominates the total energy of the universe, which will be verified to be correct later. In this case, we can derive $a \propto T^{-1}$ from the entropy conservation with $s \propto T^3$. For the numerical calculation, we define a dimensionless parameter $x \equiv m_\chi/T$. Then we can rewrite Eq. (2.5) as

$$\frac{x}{Y_{\text{eq}}} \frac{dY}{dx} = -\frac{\Gamma}{H} \left(\frac{Y^2}{Y_{\text{eq}}^2} - 1 \right), \quad (2.6)$$

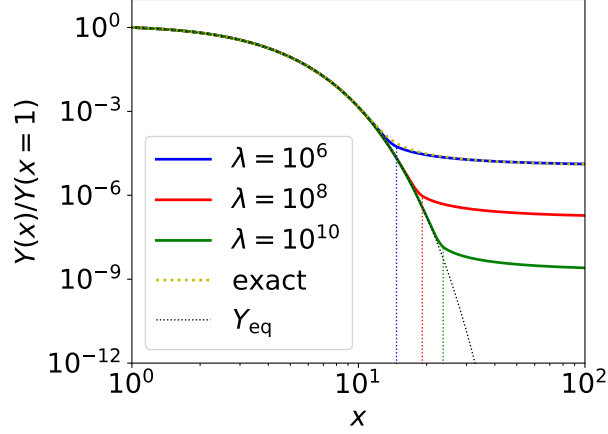


Figure 1: Plot of $Y(x)/Y(x = 1)$ with $Y(x)$ being a solution of the evolution equation Eq. (2.6). The yellow dotted line is a solution for $\lambda \equiv \Gamma/H|_{x=1} = 10^6$, while the black dotted line denotes $Y_{\text{eq}}(x)/Y_{\text{eq}}(x = 1)$. The solid lines are the approximation to the solutions described in the text. The blue, red, and green colors correspond to $\lambda = 10^8$, 10^{10} , and 10^{12} , respectively. The vertical dotted lines denote the freezeout temperature x_f .

where Γ denotes the DM interaction rate defined as

$$\Gamma \equiv n_{\text{eq}} \langle \sigma v \rangle. \quad (2.7)$$

Finally, $\langle \sigma v \rangle$ is known to be expanded as [9]

$$\langle \sigma v \rangle = \langle \sigma v \rangle_s + \langle \sigma v \rangle_p x^{-1} + \dots, \quad (2.8)$$

corresponding to the s -wave, p -wave, and so on, contributions to the cross section. When $x \gg 1$, the term with the highest power of x dominates the cross section. When the x^{-p} term dominates ($p \geq 0$), temperature dependence of the interaction rate is $\Gamma \propto x^{-3/2-p} e^{-x}$, while the Hubble parameter only reduces as $H \propto \rho^{1/2} \propto x^{-2}$. As a result, at some point Γ becomes smaller than H and Y freezes out as Eq. (2.6) indicates. Hereafter, we focus on the case of the s -wave domination with $\langle \sigma v \rangle_s \neq 0$ for simplicity. **(♣ What is the difference for p -wave and so on? ♣)** In Fig. 1, we show the solution of Eq. (2.6) for $\lambda \equiv \Gamma/H|_{x=1} = 10^6$ by the yellow dotted line. In the calculation, we use the boundary condition $Y(x = 1) = Y_{\text{eq}}(x = 1)$ and plot the normalized value $Y(x)/Y(x = 1)$. We also plot the function $Y_{\text{eq}}(x)/Y_{\text{eq}}(x = 1)$ by the black dotted line.

Unfortunately, it is computationally hard to solve Eq. (2.6) for larger values of λ because of the almost complete cancellation between two terms of the right handed side for small $x \sim \mathcal{O}(1)$ and its amplification caused by large λ . We adopt instead to use an approximation that is the same with the one adopted in the public code `MicrOMEGAs` [10, 11]. For the small

x region, temperature is still high enough to maintain the equilibrium $Y \simeq Y_{\text{eq}}$, which means that $d\Delta Y/dx \ll dY_{\text{eq}}/dx$ with $\Delta Y \equiv Y - Y_{\text{eq}}$. From this approximation we obtain a formula

$$\Delta Y \simeq -\frac{x}{2\lambda} \frac{dY_{\text{eq}}}{dx}. \quad (2.9)$$

Then we define the time x_f , or equivalently the so-called freezeout temperature T_f , when the approximation becomes invalid through the equation

$$\Delta Y(x_f) = 2.5Y_{\text{eq}}(x_f). \quad (2.10)$$

After the freezeout $x > x_f$, the annihilation of the DM pairs rapidly slows down and the DM abundance far exceeds its equilibrium value: $Y \gg Y_{\text{eq}}$. Then we can neglect the second term of the right hand of Eq. (2.6) and obtain the analytical solution

$$Y(x) \simeq -\frac{x}{c_1 x + \lambda/Y_{\text{eq}}(x=1)}, \quad (2.11)$$

where c_1 is a integration constant. In Fig. 1, we show results obtained with these two approximations Eqs. (2.9) and (2.11) for $\lambda = 10^6$ (blue), 10^8 (red), and 10^{10} (green). In particular, the blue and the yellow lines almost completely overlaps with each other, which proves the validity of the approximations. The vertical dotted lines in the figure show the freezeout temperature. It can be seen from the figure that $x = x_f$ does correspond to the time when Y starts to deviate from Y_{eq} . Note also that as $\lambda \propto \langle\sigma v\rangle$ becomes larger, the freezeout time becomes later and the late time relic abundance becomes smaller.

When the DM properties (*i.e.*, the mass m_χ and the annihilation cross section $\langle\sigma v\rangle$) are given, corresponding relic abundance can be calculated using above procedure. In particular, m_χ determines the normalization of the figure, namely $Y_{\text{eq}}(x=1) = Y_{\text{eq}}(T = m_\chi)$, and $\langle\sigma v\rangle$ determines the freezeout temperature through the combination of Eq. (2.7). Assuming the absence of non-thermal effect, only some good combination of these two values should explain the current relic abundance of the DM. From the numerical calculation, we obtain an order estimation formula

$$\Omega_\chi h^2 \sim \frac{3 \times 10^{-27} \text{ cm}^3/\text{s}}{\langle\sigma v\rangle_0} \sim 0.1 \left(\frac{0.01}{\alpha} \right)^2 \left(\frac{m_\chi}{300 \text{ GeV}} \right)^2, \quad (2.12)$$

where the rough estimation $\langle\sigma v\rangle \sim \alpha^2/m_\chi^2$ is used in the last equation with α being the fine structure constant for the DM-SM coupling. What is fascinating in Eq. (2.12) is that an object can be a DM candidate if it has mass comparable to the electroweak scale and coupling constant comparable to the electroweak coupling constant. This is the so-called *WIMP miracle*, which support the hypothesis of the WIMP as a candidate of the DM. Such TeV-scale WIMPs are theoretically well-motivated in connection with problems of the SM such as the naturalness problem. Several examples are briefly reviewed in the next section.

| WIMP DM candidate | Quntum numbers | | | Masses | |
|-------------------|----------------|----------|------------------|---------------------|----------------------------|
| | $SU(2)_L$ | $U(1)_Y$ | Spin | m_χ/TeV | $\Delta m_\chi/\text{MeV}$ |
| Higgsino | 2 | 1/2 | Dirac fermion | 1.1 | 341 |
| Wino | 3 | 0 | Majorana fermion | 2.9 | 166 |
| 5-plet scalar | 5 | 0 | real scalar | 9.4 | 166 |
| 5-plet fermion | 5 | 0 | Majorana fermion | 10 | 166 |

Table 1: Table of properties of popular WIMP DM candidates [12–17]. The $SU(2)_L$ electroweak charge, $U(1)_Y$ hypercharge, spin nature, mass, and mass difference compared with a charged component of the multiplet are shown. See Sec. ?? (♣ **Caution!!** ♣) for the details of the last column.

2.2 Brief review of models

There are several examples of the models that contain WIMP DM candidates. In this subsection, two of them (♣ **Really?** ♣) are briefly reviewed. (♣ **EWIMP and WIMP??** ♣)

Minimally supersymmetric standard model (MSSM)

(♣ **Relationship between λ parameter above should be clearer** ♣) WIMPs with mass around or just above the electroweak scale are theoretically well-motivated in connection with problems of the SM such as the naturalness problem. For example, the minimal supersymmetric extension of the SM (the so-called MSSM) contains several WIMP DM candidate such as Higgsino and Wino.^{‡2} Another example is the minimal dark matter (MDM) model [15, 19, 20], which is a simple extension of the SM with an $SU(2)_L$ electroweak multiplet such as a 5-plet scalar / fermion. In these models, the stability of the DM is ensured by the R -parity (for the MSSM case) and by high dimensionality of the operator that describes the decay of the DM (for the MDM case). The properties of these WIMP DM candidates are summarized in Table 1. The required masses to explain the DM relic abundance through the freezeout mechanism are also shown. Since the non-relativistic annihilation cross section of TeV mass particles is significantly enhanced by the Sommerfeld enhancement effect [14, 21], there are deviations from the rough estimation formula Eq. (2.12). We will return to this point later in Sec. ??. (♣ **Caution!!** ♣) In addition, in the last column there are mass differences Δm_χ between the DM and its charged counterpart that will be explained in detail in Sec. ??. (♣ **Caution!!** ♣)

^{‡2}For a review of the MSSM, see for example [18].

2.3 WIMP DM search : indirect detection

Section 3

Probing EWIMPs with Drell-Yan process at 100 TeV colliders

3.1 EWIMP effect on the lepton production processes

We investigate contributions of the EWIMPs to the Drell-Yan process through the vacuum polarization of the electroweak gauge bosons at the loop level. Throughout the paper, we assume that all the other beyond the SM particles are heavy enough so that they do not affect the following discussion. After integrating out the EWIMPs, the effective lagrangian is expressed as

$$\mathcal{L}_{\text{eff}} = \mathcal{L}_{\text{SM}} + C_2 g^2 W_{\mu\nu}^a f\left(-\frac{D^2}{m^2}\right) W^{a\mu\nu} + C_1 g'^2 B_{\mu\nu} f\left(-\frac{\partial^2}{m^2}\right) B^{\mu\nu}, \quad (3.1)$$

where \mathcal{L}_{SM} is the SM Lagrangian, D is a covariant derivative, m is the EWIMP mass,^{‡3} g and g' are the $SU(2)_L$ and $U(1)_Y$ gauge coupling constants, and $W_{\mu\nu}^a$ and $B_{\mu\nu}$ are the field strength associated with the $SU(2)_L$ and $U(1)_Y$ gauge group, respectively. The function $f(x)$ is defined as^{‡4}

$$f(x) = \begin{cases} \frac{1}{16\pi^2} \int_0^1 dy y(1-y) \ln(1 - y(1-y)x - i0) & \text{(Fermion),} \\ \frac{1}{16\pi^2} \int_0^1 dy (1-2y)^2 \ln(1 - y(1-y)x - i0) & \text{(Scalar),} \end{cases} \quad (3.2)$$

where the first (second) line corresponds to a fermionic (scalar) EWIMP, respectively. The coefficients C_1 and C_2 for an $SU(2)_L$ n -plet EWIMP with hypercharge Y are given by

$$C_1 = \frac{\kappa}{8} n Y^2, \quad (3.3)$$

$$C_2 = \frac{\kappa}{8} I(n), \quad (3.4)$$

where $\kappa = 1, 2, 8, 16$ for a real scalar, a complex scalar, a Weyl or Majorana fermion, and a Dirac fermion, respectively. The Dynkin index $I(n)$ for the n dimensional representation of

^{‡3}Here we neglect a small mass splitting among the $SU(2)_L$ multiplet.

^{‡4}If an EWIMP interacts only through the electroweak interaction, its decay width is of $O(1)\%$ or less of its mass even if it is unstable. We assume that this is the case, and neglect the small effect on the function $f(x)$ due to the small decay width.

| Fermion f | $v_f^{(\gamma)}$ | $a_f^{(\gamma)}$ | $v_f^{(Z)}$ | $a_f^{(Z)}$ | $v_f^{(W)}$ | $a_f^{(W)}$ |
|-----------------|------------------|------------------|--|-------------------|------------------------|-------------------------|
| up-type quark | $\frac{2}{3}e$ | 0 | $(\frac{1}{4} - \frac{2}{3}s_W^2)g_Z$ | $-\frac{1}{4}g_Z$ | $\frac{1}{2\sqrt{2}}g$ | $-\frac{1}{2\sqrt{2}}g$ |
| down-type quark | $-\frac{1}{3}e$ | 0 | $(-\frac{1}{4} + \frac{1}{3}s_W^2)g_Z$ | $\frac{1}{4}g_Z$ | $\frac{1}{2\sqrt{2}}g$ | $-\frac{1}{2\sqrt{2}}g$ |
| lepton | $-e$ | 0 | $(-\frac{1}{4} + s_W^2)g_Z$ | $\frac{1}{4}g_Z$ | $\frac{1}{2\sqrt{2}}g$ | $-\frac{1}{2\sqrt{2}}g$ |

Table 2: Coefficients of the weak interaction defined as $\Gamma_f^{(V)} \equiv v_f^{(V)} + a_f^{(V)}\gamma_5$. Here, $e = g_{SW}$ and $g_Z = g/c_W$, where $s_W \equiv \sin \theta_W$ and $c_W \equiv \cos \theta_W$ with θ_W being the weak mixing angle.

$SU(2)_L$ is given by

$$I(n) = \frac{1}{12}(n^3 - n), \quad (3.5)$$

which is normalized so that $I(2) = 1/2$. The coefficients are uniquely determined by the representation of the EWIMPs. For example, $(C_1, C_2) = (1, 1)$ for Higgsino, and $(C_1, C_2) = (0, 2)$ for Wino. We emphasize that, contrary to the usual effective field theory, our prescription is equally applied when the typical scale of the gauge boson four-momentum, q , is larger than the EWIMP mass scale m since we do not perform a derivative expansion of f in Eq. (3.1). It is important because, as we see soon, the effect of the EWIMPs are maximized when $\sqrt{q^2} \sim m$, where the derivative expansion is not applicable.

At the leading order (LO), we are interested in $u(p) \bar{u}(p') \rightarrow \ell^-(k) \ell^+(k')$ and $d(p) \bar{d}(p') \rightarrow \ell^-(k) \ell^+(k')$ as the NC processes and $u(p) \bar{d}(p') \rightarrow \nu(k) \ell^+(k')$ and $d(p) \bar{u}(p') \rightarrow \ell^-(k) \bar{\nu}(k')$ as the CC processes. Here, u and d collectively denote up-type and down-type quarks, respectively, and p, p', k , and k' are initial and final state momenta. In the SM, the amplitudes for both the NC and CC processes at the LO are expressed as

$$\mathcal{M}_{\text{SM}} = \sum_V \frac{\left[\bar{v}(p') \gamma^\mu \Gamma_q^{(V)} u(p) \right] \left[\bar{u}(k) \gamma_\mu \Gamma_\ell^{(V)} v(k') \right]}{s' - m_V^2}, \quad (3.6)$$

where $\sqrt{s'}$ is the invariant mass of the final state leptons, which is denoted as $m_{\ell\ell}$ for the NC processes and $m_{\ell\nu}$ for the CC processes. The relevant gauge bosons are $V = \gamma, Z$ for the NC processes and $V = W^\pm$ for the CC processes, with m_V being the corresponding gauge boson mass. In addition,

$$\Gamma_f^{(V)} \equiv v_f^{(V)} + a_f^{(V)}\gamma_5, \quad (3.7)$$

with $v_f^{(V)}$ and $a_f^{(V)}$ given in Tab. 2. The EWIMP contribution is given by

$$\mathcal{M}_{\text{EWIMP}} = \sum_{V, V'} C_{VV'} s' f\left(\frac{s'}{m^2}\right) \frac{\left[\bar{v}(p') \gamma^\mu \Gamma_q^{(V)} u(p) \right] \left[\bar{u}(k) \gamma_\mu \Gamma_\ell^{(V')} v(k') \right]}{(s' - m_V^2)(s' - m_{V'}^2)}, \quad (3.8)$$

where $C_{\gamma\gamma} = 4(C_1 g'^2 c_W^2 + C_2 g^2 s_W^2)$, $C_{\gamma Z} = C_{Z\gamma} = 4(C_2 g^2 - C_1 g'^2) s_W c_W$, $C_{ZZ} = 4(C_1 g'^2 s_W^2 + C_2 g^2 c_W^2)$, and $C_{WW} = 4C_2 g^2$. Again $V, V' = \gamma, Z$ for the NC processes and $V, V' = W^\pm$ for the CC processes.

We use $d\Pi_{\text{LIPS}}$ for a Lorentz invariant phase space factor for the two particles final state. Then, using Eqs. (3.6) and (3.8), we define

$$\frac{d\sigma_{\text{SM}}}{d\sqrt{s'}} = \sum_{a,b} \frac{dL_{ab}}{d\sqrt{s'}} \int d\Pi_{\text{LIPS}} |\mathcal{M}_{\text{SM}}(q_a \bar{q}_b \rightarrow \ell\ell/\ell\nu)|^2, \quad (3.9)$$

$$\frac{d\sigma_{\text{EWIMP}}}{d\sqrt{s'}} = \sum_{a,b} \frac{dL_{ab}}{d\sqrt{s'}} \int d\Pi_{\text{LIPS}} 2\Re[\mathcal{M}_{\text{SM}}\mathcal{M}_{\text{EWIMP}}^*(q_a \bar{q}_b \rightarrow \ell\ell/\ell\nu)], \quad (3.10)$$

where we take the average and summation over spins. Here, $dL_{ab}/d\sqrt{s'}$ is the luminosity function for a fixed $\sqrt{s'}$:

$$\frac{dL_{ab}}{d\sqrt{s'}} \equiv \frac{1}{s} \int_0^1 dx_1 dx_2 f_a(x_1) f_b(x_2) \delta\left(\frac{s'}{s} - x_1 x_2\right), \quad (3.11)$$

where a and b denote species of initial partons, \sqrt{s} is the center of mass energy of the proton collision ($\sqrt{s} = 100$ TeV in our case), and $f_a(x)$ is a parton distribution function (PDF) of the given parton a . Eq. (3.9) represents the SM cross section, while Eq. (3.10) the EWIMP contribution to the cross section. For the statistical treatment in the next section, we introduce a parameter μ that parametrizes the strength of the EWIMP effect, and express the cross section with μ as

$$\frac{d\tilde{\sigma}}{d\sqrt{s'}} = \frac{d\sigma_{\text{SM}}}{d\sqrt{s'}} + \mu \frac{d\sigma_{\text{EWIMP}}}{d\sqrt{s'}}. \quad (3.12)$$

Obviously, $\mu = 0$ corresponds to the pure SM, while $\mu = 1$ corresponds to the SM+EWIMP model. Hereafter, we use

$$\delta_\sigma(\sqrt{s'}) \equiv \frac{d\sigma_{\text{EWIMP}}/d\sqrt{s'}}{d\sigma_{\text{SM}}/d\sqrt{s'}}, \quad (3.13)$$

to denote the correction from the EWIMP.

In Fig. 2, we plot δ_σ for the CC processes as a function of $\sqrt{s'}$. The purple, blue, and red lines correspond to Higgsino, Wino, and 5-plet scalar, respectively. There is a dip around $\sqrt{s'} = 2m$ for all the cases of the EWIMPs which originates from the loop function f in Eq. (3.2). The EWIMP contributions to the NC processes show a similar dip structure that again comes from f . This dip is crucial not only for the discovery of the EWIMP signal (see Sec. 3.2.3) but also for the determination of the properties of the EWIMPs (see Sec. 3.2.4). In particular, the EWIMP mass can be extracted from the dip position, while the EWIMP charges (n and Y) can be determined from the depth of the dip.

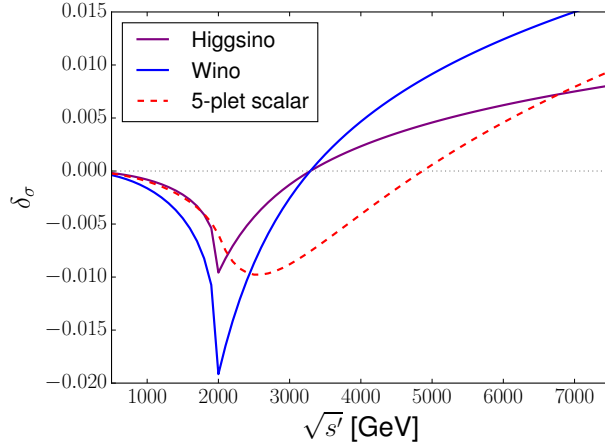


Figure 2: δ_σ for the CC processes as a function of $\sqrt{s'} = m_{\ell\nu}$. The purple, blue, and red lines correspond to Higgsino, Wino, and 5-plet real scalar, respectively.

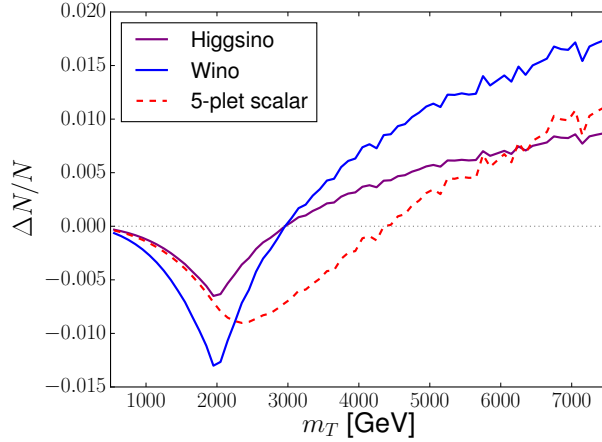


Figure 3: The EWIMP effect on the ratio of the number of events $\Delta N/N$ as a function of m_T . The line colors are the same as Fig. 2.

For the NC processes, the momenta of two final state charged leptons are measurable and we can use the invariant mass distribution of the number of events for the study of the EWIMPs. For the CC processes, on the contrary, we cannot measure the momentum of the neutrino in real experiments, and hence we instead use the missing transverse momentum $p_{T,\text{miss}}$. We use the transverse mass defined as

$$m_T^2 \equiv 2p_{T,\ell} p_{T,\text{miss}} (1 - \cos(\phi_{T,\ell,\text{miss}})), \quad (3.14)$$

where $p_{T,\ell}$ denotes the transverse momentum of the charged lepton and $\phi_{T,\ell,\text{miss}} \equiv \phi_\ell - \phi_{\text{miss}}$ is the difference between the azimuth angles of $p_{T,\ell}$ and $p_{T,\text{miss}}$. The important property

of m_T is that the distribution of m_T peaks at $m_T = m_{\ell\nu}$. Because of this property, the characteristic shape of δ_σ remains in the m_T distribution in the CC events. To see this, we plot in Fig. 3 the EWIMP effect on the number of events as a function of m_T . Here, the vertical axis is the ratio of the EWIMP correction to the number of events ΔN to the number of events in the SM N for each bin with the bin width of 100 GeV.⁵ We find that the dip structure remains in the m_T distribution, though the depth of the dip is smaller compared to the $m_{\ell\nu}$ distribution.

3.2 Analysis

3.2.1 Event generation

Now we discuss how well we can extract information about EWIMPs from the invariant mass and transverse mass distributions for the processes of our concern at future 100 TeV pp collider experiments. We take into account the effects of the next-to-leading order QCD corrections in the events as well as detector effects through Monte-Carlo simulations.

In our analysis, we first generate the SM event sets for the NC processes $pp \rightarrow e^-e^+/\mu^-\mu^+$ and for the CC processes $pp \rightarrow e^\pm\nu_e/\mu^\pm\nu_\mu$. We use `MadGraph5_aMC@NLO` (v2.6.3.2) [22, 23] for the event generation with the successive use of `Pythia8` [24] for the parton shower and the hadronization and `Delphes` (v3.4.1) [25] with the card `FCChh.tcl` for the detector simulation. We use `NNPDF2.3QED` with $\alpha_s(M_Z) = 0.118$ [26] as a canonical set of PDFs. For the renormalization and factorization scales, we use the default values of `MadGraph5_aMC@NLO`, i.e., the central m_T^2 scale after k_T -clustering of the event (which we denote by Q). The events are binned by the characteristic mass m_{char} for each process: we use the lepton invariant mass $m_{\text{char}} = m_{\ell\ell}$ for the NC processes, and the transverse mass $m_{\text{char}} = m_T$ for the CC processes, respectively. In both cases, we generated events with the characteristic mass within the range of $500 \text{ GeV} < m_{\text{char}} < 7.5 \text{ TeV}$ and divide them into 70 bins with the equal width of 100 GeV.

As for the event selection by a trigger, we may have to impose some cut on the lepton transverse momentum p_T . As we will see, we concentrate on events with high p_T charged lepton(s) with which we expect the event may be triggered. For the NC processes, we use events with at least two high p_T leptons. For our analysis, we use events with $m_{\ell\ell} > 500 \text{ GeV}$; we assume that such events are triggered by using two energetic charged leptons so that we do not impose extra kinematical requirements. On the contrary, the CC events are characterized only by a lepton and a missing transverse momentum. For such events, we require that the

⁵Just for an illustrative purpose, we generate events corresponding to the integrated luminosity $\mathcal{L} = 1 \text{ ab}^{-1}$ for this figure, which is not the same luminosity as we use in the next section (see Sec. 3.2.1 for details of the event generation).

p_T of the charged lepton should be larger than 500 GeV.^{‡6} For the CC events, the cut reduces the number of events in particular for the bins with the low transverse mass $m_T \sim 500$ GeV, and thus affects the sensitivity of the CC processes to relatively light EWIMPs. We will come back to this point later.

The EWIMP effect is incorporated by rescaling the SM event by δ_σ defined in Eq. (3.13). With the parameter μ defined in Eq. (3.12), the number of events corresponding to the SM+EWIMP hypothesis in i -th bin, characterized by $m_{i,\min} < m_{\text{char}} < m_{i,\max}$, is

$$x_{f,i}(\mu) = \sum_{m_{i,\min} < m_{\text{char}} < m_{i,\max}} \left[1 + \mu \delta_\sigma(\sqrt{s'}) \right], \quad (3.1)$$

where the sum runs over all the events of the final state f whose characteristic mass m_{char} (after taking into account the detector effects) falls into the bin. Note that the true value of $\sqrt{s'}$ should be used for each event for the computation of δ_σ : we extract it from the hard process information.^{‡7}

3.2.2 Statistical treatment

We now explain the statistical method we will adopt in our analysis. We collectively denote our theoretical model as $\mathbf{x}_f(\mu) = \{x_{f,i}(\mu)\}$, where $x_{f,i}(\mu)$ is given by Eq. (3.1). We denote the experimental data set as $\tilde{\mathbf{x}}_f$ that in principle is completely unrelated to our theoretical model $\mathbf{x}_f(\mu)$. Since we do not have an actual experimental data set for 100 TeV colliders for now, however, we take $\tilde{\mathbf{x}}_f = \mathbf{x}_f(\mu = 1)$ (for some fixed values of the EWIMP mass and charges) throughout our analysis, assuming that the EWIMP does exist. In particular, this choice tests the SM-only hypothesis if we take our theoretical model as $\mathbf{x}_f(\mu = 0)$.

If the expectation values of $x_{f,i}(\mu)$ are precisely known, the sensitivity to EWIMPs can be studied only with statistical errors. In reality, however, the computation of $x_{f,i}(\mu)$ suffers various sources of uncertainties, which results in systematic errors in our theoretical model. The sources include errors in the integrated luminosity, the beam energy, choices of the renormalization and the factorization scales, choices of PDF, the pile-up effect, higher order corrections to the cross section, and so on. In order to deal with these uncertainties, we introduce sets of free parameters $\boldsymbol{\theta}_f = \{\theta_{f,\alpha}\}$ (i.e. nuisance parameters) which absorb (smooth) uncertainties of the number of events, and modify our theoretical model as

$$\tilde{x}_{f,i}(\boldsymbol{\theta}_f, \mu) \equiv x_{f,i}(\mu) f_{\text{sys},i}(\boldsymbol{\theta}_f), \quad (3.2)$$

^{‡6}In the ATLAS analysis of the mono-lepton signal during the 2015 (2016) data taking period [27], they use the event selection condition $p_T > 24$ (60) GeV for leptons that satisfy the *medium* identification criteria. In the CMS analysis during the period on 2016 [28], they use the condition $p_T > 130$ (53) GeV for an electron (a muon).

^{‡7}The p_T cut for the CC process does not affect this estimation since the EWIMP does not modify the angular distribution of the final lepton and neutrino for the CC process.

where $f_{\text{sys},i}(\boldsymbol{\theta}_f)$ is a function that satisfies $f_{\text{sys},i}(\mathbf{0}) = 1$. We expect that, if the function $f_{\text{sys},i}$ is properly chosen, the true distribution of the number of events in the SM is given by $\tilde{\mathbf{x}}_f(\boldsymbol{\theta}_f, 0) = \{\tilde{x}_{f,i}(0)f_{\text{sys},i}(\boldsymbol{\theta}_f)\}$ for some value of $\boldsymbol{\theta}_f$. In our analysis, we adopt the five parameters fitting function given by [29]

$$f_{\text{sys},i}(\boldsymbol{\theta}_f) = e^{\theta_{f,1}}(1 - p_i)^{\theta_{f,2}}p_i^{(\theta_{f,3} + \theta_{f,4} \ln p_i + \theta_{f,5} \ln^2 p_i)}, \quad (3.3)$$

where $p_i = 2m_i/\sqrt{s}$ with m_i being the central value of the lepton invariant mass (transverse mass) of the i -th bin for the NC (CC) processes. As we will see, the major effects of systematic errors can be absorbed into $\boldsymbol{\theta}_f$ with this fitting function.

In order to test the SM-only hypothesis, we define the following test statistic [30]:

$$q_0 \equiv -2 \sum_{f=\ell\ell, \ell\nu} \ln \frac{L(\tilde{\mathbf{x}}_f; \hat{\boldsymbol{\theta}}_f, \mu = 0)}{L(\tilde{\mathbf{x}}_f; \hat{\boldsymbol{\theta}}_f, \hat{\mu})}. \quad (3.4)$$

Here, $\hat{\boldsymbol{\theta}}_f$ and $\{\hat{\boldsymbol{\theta}}_f, \hat{\mu}\}$ are determined so that $\prod_f L(\tilde{\mathbf{x}}_f; \boldsymbol{\theta}_f, \mu = 0)$ and $\prod_f L(\tilde{\mathbf{x}}_f; \boldsymbol{\theta}_f, \mu)$ are maximized, respectively. The likelihood function is defined as

$$L(\tilde{\mathbf{x}}_f; \boldsymbol{\theta}_f, \mu) \equiv L_{\boldsymbol{\theta}_f}(\tilde{\mathbf{x}}_f; \mu) L'(\boldsymbol{\theta}_f; \boldsymbol{\sigma}_f), \quad (3.5)$$

where

$$L_{\boldsymbol{\theta}_f}(\tilde{\mathbf{x}}_f; \mu) \equiv \prod_i \exp \left[-\frac{(\tilde{x}_{f,i} - \tilde{x}_{f,i}(\boldsymbol{\theta}_f, \mu))^2}{2\tilde{x}_{f,i}(\boldsymbol{\theta}_f, \mu)} \right], \quad (3.6)$$

$$L'(\boldsymbol{\theta}_f; \boldsymbol{\sigma}_f) \equiv \prod_{\alpha} \exp \left[-\frac{\theta_{f,\alpha}^2}{2\sigma_{f,\alpha}^2} \right]. \quad (3.7)$$

The product in Eq. (3.6) runs over all the bins, while the product in Eq. (3.7) runs over all the free parameters we introduced. For each $\theta_{f,\alpha}$, we define the “standard deviation” $\sigma_{f,\alpha}$, which parametrizes the possible size of $\theta_{f,\alpha}$ within the SM with the systematic errors.^{‡8} If the systematic errors are negligible compared with the statistical error, we can take $\boldsymbol{\sigma}_f \rightarrow \mathbf{0}$, while the analysis with $\boldsymbol{\sigma}_f \rightarrow \infty$ assumes no knowledge of systematic errors and gives a conservative result. We identify $(q_0)^{1/2} = 5$ (1.96) as the detection reach at the 5σ (95 % C.L.) level, since q_0 asymptotically obeys a chi-square distribution with the degree of freedom one.

In order to determine $\boldsymbol{\sigma}_f$, we consider the following sources of the systematic errors:

- Luminosity ($\pm 5\%$ uncertainty is assumed),

^{‡8}Here we assume the Gaussian form for the nuisance parameter distribution. The dependence of the results on the choice of the distribution will be discussed later in Sec. 3.2.3.

- Renormalization scale ($2Q$ and $Q/2$, instead of Q),
- Factorization scale ($2Q$ and $Q/2$, instead of Q),
- PDF choice (We use 101 variants of NNPDF2.3QED with $\alpha_s(M_Z) = 0.118$ [26] provided by LHAPDF6 [31] with IDs ranging from 244600 to 244700).

The values of σ_f are determined as follows. Let \mathbf{y}_f be the set of number of events in the SM for the final state f with the canonical choices of the parameters, and \mathbf{y}'_f be that with one of the sources of the systematic errors being varied. We minimize the chi-square function defined as

$$\chi_f^2 \equiv \sum_i \frac{(y'_{f,i} - \tilde{y}_{f,i}(\boldsymbol{\theta}_f))^2}{\tilde{y}_{f,i}(\boldsymbol{\theta}_f)}, \quad (3.8)$$

where

$$\tilde{y}_{f,i}(\boldsymbol{\theta}_f) \equiv y_{f,i} f_{\text{sys},i}(\boldsymbol{\theta}_f), \quad (3.9)$$

for each final state f , and determine the best-fit values of $\boldsymbol{\theta}_f$ for each set of \mathbf{y}'_f . We repeat this process for different sets of \mathbf{y}'_f , and σ_f are determined from the distributions of the best-fit values of $\boldsymbol{\theta}_f$. For example, let us denote the best-fit values for the fit associated with the luminosity errors $\pm 5\%$ as $\boldsymbol{\theta}_f^\pm$. We estimate σ_f associated with these errors, denoted here as $\sigma_f^{\text{lumi.}}$, as

$$\sigma_{f,\alpha}^{\text{lumi.}} = \sqrt{\frac{(\theta_{f,\alpha}^+)^2 + (\theta_{f,\alpha}^-)^2}{N}}, \quad (3.10)$$

where N denotes the number of fitting procedures we have performed: $N = 2$ for this case. We estimate σ_f associated with the other sources of the errors, denoted as $\sigma_f^{\text{ren.}}$, $\sigma_f^{\text{fac.}}$, and σ_f^{PDF} , in a similar manner. Finally, the total values of σ_f are obtained by combining all the sources together as^{‡9}

$$\sigma_{f,\alpha} = \sqrt{(\sigma_{f,\alpha}^{\text{lumi.}})^2 + (\sigma_{f,\alpha}^{\text{ren.}})^2 + (\sigma_{f,\alpha}^{\text{fac.}})^2 + (\sigma_{f,\alpha}^{\text{PDF}})^2}. \quad (3.11)$$

In Tables 3 and 4, we show the values of σ_{ee} and $\sigma_{e\nu_e}$ associated with each source of the systematic errors, respectively. These values can be interpreted as the possible size of the fit parameters within the SM, which is caused by the systematic uncertainties. As explained in Eq. (3.11), we combine these values in each column to obtain σ_f . In Table 5, we summarize

^{‡9}There may be some correlations between the distribution of nuisance parameters $\boldsymbol{\theta}_f$. In this paper, we treat each of them as obeying to an independent Gaussian distribution for simplicity.

| Sources of systematic errors | $\sigma_{ee,1}$ | $\sigma_{ee,2}$ | $\sigma_{ee,3}$ | $\sigma_{ee,4}$ | $\sigma_{ee,5}$ |
|--|-----------------|-----------------|-----------------|-----------------|-----------------|
| Luminosity: $\pm 5\%$ ($\sigma_{ee}^{\text{lumi.}}$) | 0.05 | 0 | 0 | 0 | 0 |
| Renormalization scale: $2Q, Q/2$ ($\sigma_{ee}^{\text{ren.}}$) | 0.4 | 0.6 | 0.3 | 0.05 | 0.004 |
| Factorization scale: $2Q, Q/2$ ($\sigma_{ee}^{\text{fac.}}$) | 0.3 | 0.5 | 0.2 | 0.06 | 0.004 |
| PDF choice (σ_{ee}^{PDF}) | 0.4 | 0.7 | 0.3 | 0.06 | 0.004 |

Table 3: Values of σ_{ee} for each source of systematic errors. The result is the same for the $\mu\mu$ final state.

| Sources of systematic errors | $\sigma_{e\nu_e,1}$ | $\sigma_{e\nu_e,2}$ | $\sigma_{e\nu_e,3}$ | $\sigma_{e\nu_e,4}$ | $\sigma_{e\nu_e,5}$ |
|--|---------------------|---------------------|---------------------|---------------------|---------------------|
| Luminosity: $\pm 5\%$ ($\sigma_{e\nu_e}^{\text{lumi.}}$) | 0.05 | 0 | 0 | 0 | 0 |
| Renormalization scale: $2Q, Q/2$ ($\sigma_{e\nu_e}^{\text{ren.}}$) | 0.3 | 0.4 | 0.2 | 0.04 | 0.003 |
| Factorization scale: $2Q, Q/2$ ($\sigma_{e\nu_e}^{\text{fac.}}$) | 1.0 | 1.6 | 0.6 | 0.1 | 0.01 |
| PDF choice ($\sigma_{e\nu_e}^{\text{PDF}}$) | 0.6 | 0.9 | 0.4 | 0.08 | 0.006 |

Table 4: Best fit values of fit parameters for several sources of systematic errors for the $e\nu_e$ final state. The result is the same for the $\mu\nu_\mu$ final state.

the result of the combination for all the final states. The values of σ_f are independent of the final state lepton flavors since the energy scale of our concern is much higher than the lepton masses. However, we use different sets of fit parameters θ_{ee} and $\theta_{\mu\mu}$ for the NC processes and $\theta_{e\nu_e}$ and $\theta_{\mu\nu_\mu}$ for the CC processes because of the different detector response to electrons and muons.

In the tables, we have neglected the systematic errors from the detector effect. The main errors are expected to come from the lepton identification, in which some of the leptons in any process are overlooked or identified incorrectly, resulting in the misreconstruction of the event topology. Since we perform the fitting procedure as Eq. (3.4), it is expected that the small and smooth modification of the number of events as a function of the lepton invariant mass may be absorbed into the choice of nuisance parameters, if the corresponding values of σ_f are properly taken into account in addition to the values in Table 3. What is dangerous is the possible jerky modification that mimics the EWIMP signal, which may be induced by the detector setup, the complicated detector response to leptons, and so on. In this paper, we just assume that these systematic errors from the detector effect are well controlled once the real experiment will start and focus on the theoretical uncertainties listed in tables.

| Final state f | $\sigma_{f,1}$ | $\sigma_{f,2}$ | $\sigma_{f,3}$ | $\sigma_{f,4}$ | $\sigma_{f,5}$ |
|-----------------|----------------|----------------|----------------|----------------|----------------|
| ee | 0.7 | 1.0 | 0.4 | 0.09 | 0.008 |
| $\mu\mu$ | 0.7 | 1.0 | 0.4 | 0.09 | 0.008 |
| $e\nu_e$ | 1.2 | 1.9 | 0.7 | 0.2 | 0.01 |
| $\mu\nu_\mu$ | 1.2 | 1.9 | 0.7 | 0.2 | 0.01 |

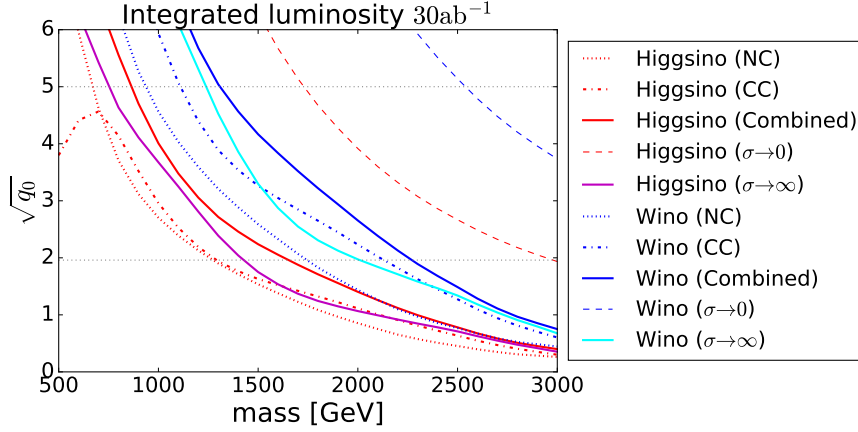
Table 5: Summary of standard deviations σ_f for each final state.

Figure 4: $\sqrt{q_0}$ as a function of the EWIMP mass. Red and blue lines correspond to the Higgsino and Wino, respectively, while line styles represent the result from the NC processes, the CC processes, the combined analysis, and the combined analysis with the optimistic $\sigma_f \rightarrow 0$ limit. The purple and cyan lines correspond to the results from the conservative analysis with $\sigma_f \rightarrow \infty$ for the Higgsino and Wino, respectively.

3.2.3 Detection reach

Now we show the detection reach of EWIMPs at future 100 TeV colliders. In Fig. 4, we plot the value of $\sqrt{q_0}$ as a function of the EWIMP mass, with the integrated luminosity $\mathcal{L} = 30 \text{ ab}^{-1}$. As representative scenarios, we show the cases for Higgsino (the red lines) and Wino (the blue lines). The dotted and dash-dotted lines are the result obtained only from the NC processes and the CC processes, respectively. We find that the CC processes are more sensitive to the effect of the EWIMPs than the NC processes because of the larger cross section. This result is consistent with Refs. [32, 33]. The sensitivity of the CC processes is weakened for $m \lesssim 700 \text{ GeV}$ because of the lepton p_T cut we have applied.^{‡10} The combined

^{‡10}We note here that the sensitivity of the CC processes depends on the lepton p_T cut. For example, adopting the tighter cut, lepton- $p_T > 1 \text{ TeV}$, the CC processes have almost no sensitivity to EWIMPs with $m < 1 \text{ TeV}$. Thus, in particular for the purpose of the Higgsino search, it is important to realize the lepton

results of the NC and CC processes are shown by the solid lines. By combining the two types of processes, the 5σ discovery reaches (95 % C.L. bounds) for Higgsino and Wino are 850 GeV (1.7 TeV) and 1.3 TeV (2.3 TeV), respectively. We find that the combination of the NC and CC processes improves the sensitivity of the EWIMP mass. Furthermore, if we understand all the systematic uncertainties quite well and effectively take the $\sigma_f \rightarrow \mathbf{0}$ limit in the combined result, the detection reach will be pushed up significantly as shown by the dashed lines: 1.1 TeV Higgsino signal at well above 5σ level and a 4σ hint of the 2.9 TeV Wino. These lines should be compared with the combined results and also with those obtained from the conservative analysis with $\sigma_f \rightarrow \infty$, assuming no knowledge about sources of systematic errors. The plot shows us that it is essential to reduce the systematic uncertainties for the detection of EWIMPs through the NC and CC processes.

So far, we have adopted the assumption that the distribution of the nuisance parameters is the Gaussian form and that the fitting function Eq. (3.3) is sufficient for treating systematic errors. In order to discuss the dependence of the results on these assumptions, we have repeated the same analysis using another distribution or fitting function. In the former case, we have adopted the top-hat distribution: the likelihood function for the nuisance parameters L' is given by

$$L'(\boldsymbol{\theta}_f; \boldsymbol{\sigma}_f) \equiv \prod_{\alpha} \Theta \left(\sqrt{3} \sigma_{f,\alpha} - |\theta_{f,\alpha}| \right), \quad (3.12)$$

where Θ is the Heaviside step function. This corresponds to the top-hat distribution of $\theta_{f,\alpha}$ with the variance $\sigma_{f,\alpha}^2$ for each α . As for an example of another fitting function, we have adopted a simple one parameter extension of Eq. (3.3)

$$f_{\text{sys},i}(\boldsymbol{\theta}_f) = e^{\theta_{f,1}} (1 - p_i)^{\theta_{f,2}} p_i^{(\theta_{f,3} + \theta_{f,4} \ln p_i + \theta_{f,5} \ln^2 p_i + \theta_{f,6} \ln^3 p_i)}, \quad (3.13)$$

which consists of six parameters. The variances of the nuisance parameters are estimated in the same way as Sec. 3.2.2, but now with the six parameters.

In Fig. 5, we show the corresponding results. The convention for the line colors is the same as Fig. 4, while the line styles denote different procedures: the dashed and dotted lines correspond to the result with the top-hat distribution and that with the six parameters fitting function, respectively, while solid lines are the same as Fig. 4. From the figure, we can see that the choice of the distribution may slightly affect the result, while the addition of a nuisance parameter as Eq. (3.13) causes almost no effect. The size of the effect of the choice of the distribution for the current estimation of errors σ_f is about 100 GeV (200 GeV) for the 5σ (95 % C.L.) bounds. We expect that such uncertainties due to the procedure to include the systematic errors will be reduced once the data from the real experiment (and hence better understanding of the systematic errors) will become available.

p_T cut as low as ~ 500 GeV.

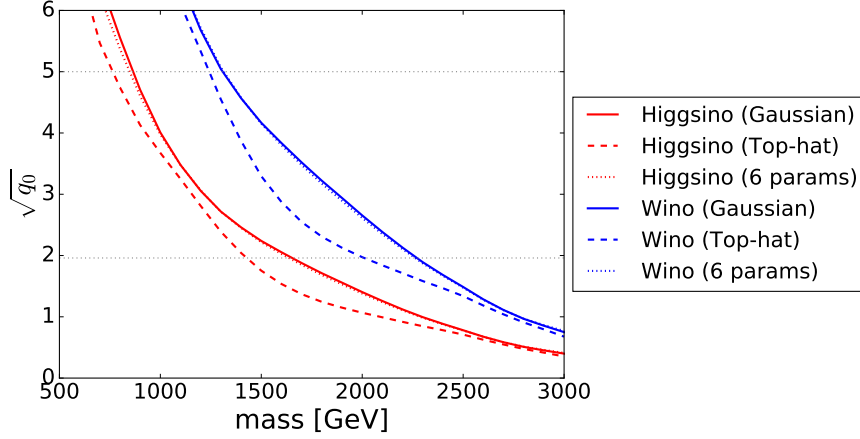


Figure 5: $\sqrt{q_0}$ as a function of the EWIMP mass using both the NC and CC processes. The convention for the line colors is the same as Fig. 4. The line styles denote the result same as Fig. 4 (solid), that with the top-hat distribution (dashed), and that with the six parameters fitting function (dotted).

3.2.4 Determination of EWIMP properties

In this subsection, we show that it is possible to determine the properties of the EWIMPs from the NC and CC processes, thanks to the fact that we can study the $m_{\ell\ell}$ and m_T distribution in great detail for these processes. Some information about the mass, charge, and spin of the EWIMPs can be extracted because the corrections to these distributions from the EWIMPs are completely determined by these EWIMP properties. Firstly, we can extract the EWIMP mass from the position of the dip-like structure in the correction since it corresponds to roughly twice the EWIMP mass as we have shown in Sec. 3.1. Secondly, the overall size of the correction gives us information about the $SU(2)_L$ and $U(1)_Y$ charges. The CC processes depend only on the $SU(2)_L$ charge, while the NC processes depend both on the $SU(2)_L$ and $U(1)_Y$ charges. Consequently, we can obtain information about the gauge charges of the EWIMPs from the NC and CC processes.

We now demonstrate the mass and charge determination of fermionic EWIMPs. This is equivalent to the determination of the parameter set (m, C_1, C_2) . We generate the data assuming the SM + EWIMP model ($\mu = 1$) with some specific values of m, n, Y , and κ , with which we obtain (m, C_1, C_2) . We fix $\mu = 1$ for our theoretical model as well, and hence the theoretical predictions of the number of events also depend on these three parameters, $\mathbf{x}_f = \mathbf{x}_f(m, C_1, C_2)$. We define the likelihood function $L(\tilde{\mathbf{x}}_f; \boldsymbol{\theta}_f, m, C_1, C_2)$ in the same form as Eqs. (3.2) and (3.5) with the theoretical prediction \mathbf{x}_f now understood as a function of

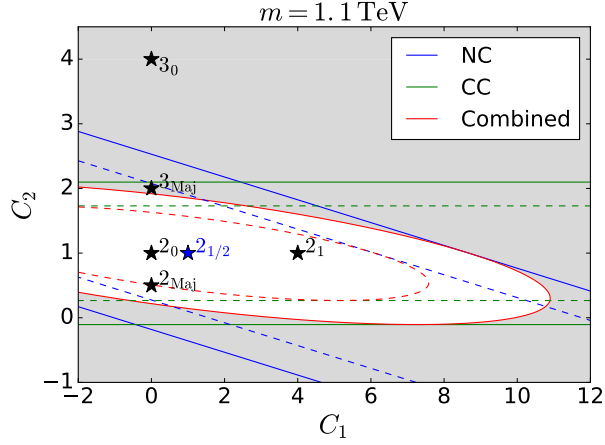


Figure 6: Contour of \sqrt{q} in the C_1 vs. C_2 plane with $m = 1.1$ TeV, where we assume 1.1 TeV Higgsino signal. The dotted and solid lines denote 1σ and 2σ contours, respectively, and the gray region corresponds to the parameter space that is in tension with the observation at more than 2σ level. The blue, green, and red lines correspond to the result from the NC processes, the CC processes, and the combined analysis, respectively. Each star marker annotated as “ n_Y ” represents a point corresponding to a $SU(2)_L$ n -plet Dirac fermion with hypercharge Y , while that with “ n_{Maj} ” corresponds to an $SU(2)_L$ n -plet Majorana fermion.

(m, C_1, C_2) , not of μ .^{‡11} The test statistic is defined as

$$q(m, C_1, C_2) \equiv -2 \sum_f \ln \frac{L(\tilde{\mathbf{x}}_f; \hat{\boldsymbol{\theta}}_f, m, C_1, C_2)}{L(\tilde{\mathbf{x}}_f; \hat{\boldsymbol{\theta}}_f, \hat{m}, \hat{C}_1, \hat{C}_2)}, \quad (3.14)$$

where the parameters $(\{\hat{\boldsymbol{\theta}}_f\}, \hat{m}, \hat{C}_1, \hat{C}_2)$ maximize $\prod_f L(\tilde{\mathbf{x}}_f; \boldsymbol{\theta}_f, m, C_1, C_2)$, while $\hat{\boldsymbol{\theta}}_f$ maximize $L(\tilde{\mathbf{x}}_f; \boldsymbol{\theta}_f, m, C_1, C_2)$ for fixed values of (m, C_1, C_2) . It follows the chi-squared distribution with three degrees of freedom in the limit of a large number of events [34]. The test statistic defined in this way examines the compatibility of a given EWIMP model (i.e. a parameter set (m, C_1, C_2)) with the observed signal.

Once a deviation from the SM prediction is observed in a real experiment, we may determine (m, C_1, C_2) using the above test statistic q . In the following, we show the expected accuracy of the determination of (m, C_1, C_2) for the case where there exists 1.1 TeV Higgsino.^{‡12}

^{‡11}As shown in Eqs. (3.3) and (3.4), C_1 and C_2 are positive quantities (and C_2 is discrete). In the figures, however, we extend the C_1 and C_2 axes down to negative regions just for presentation purposes.

^{‡12}The expected significance is 3.5σ for 1.1 TeV Higgsino in our estimation. Even though it is slightly below the 5σ discovery, we take 1.1 TeV Higgsino as an example because it is a candidate of the thermal relic DM.

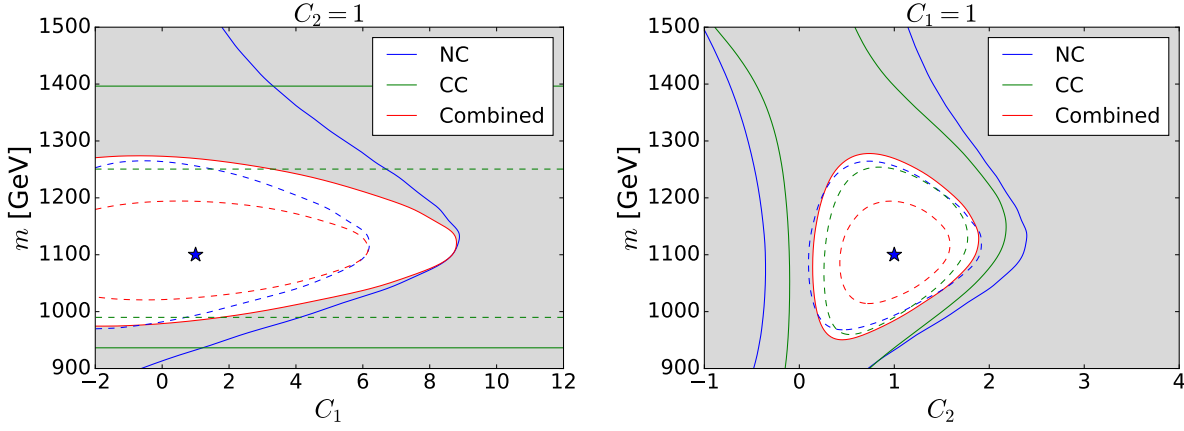


Figure 7: **Left:** Contour of \sqrt{q} in the C_1 vs. m plane with $C_2 = 1$, where we assume the 1.1 TeV Higgsino signal. The colors and styles of lines and the meaning of the gray region are the same as Fig. 6. The star marker corresponds to the true Higgsino property $(C_1, m) = (1, 1.1 \text{ TeV})$. **Right:** Contour of \sqrt{q} in the C_2 vs. m plane for $C_1 = 1$, where we assume the 1.1 TeV Higgsino signal. The star marker corresponds to the true Higgsino property $(C_2, m) = (1, 1.1 \text{ TeV})$.

In Fig. 6, we show the contours of 1σ (dotted) and 2σ (solid) constraints, which correspond to the values $\sqrt{q} = 1.9$ and $\sqrt{q} = 2.8$, respectively, in the C_1 vs. C_2 plane for $m = 1.1 \text{ TeV}$. The blue, green, and red lines denote the result obtained from the NC processes, the CC processes, and the combined analysis, respectively. The models in the gray region are in more than 2σ tension with the observation. We also show several star markers that correspond to the single $SU(2)_L$ multiplet contributions: the markers with “ n_Y ” represent an $SU(2)_L$ n -plet Dirac fermion with hypercharge Y , while those with “ n_{Maj} ” an $SU(2)_L$ n -plet Majorana fermion. Both the NC and CC constraints are represented as straight bands in the C_1 vs. C_2 plane since each process depends on a specific linear combination of C_1 and C_2 . In particular, the CC constraint is independent of C_1 , or Y . In this sense, the NC and CC processes are complementary to each other, and thus we can separately constrain C_1 and C_2 only after combining these two results. For instance, we can exclude a single fermionic $SU(2)_L$ multiplet with $n \neq 2$ at more than 2σ level, although each process by itself cannot exclude the possibility of 3_{Maj} . We can also constrain the hypercharge, yet it is not uniquely determined. In addition to the Higgsino, the EWIMP as an $SU(2)_L$ doublet Dirac fermion with $|Y|^2 \lesssim 2$ or an $SU(2)_L$ doublet Majorana fermion with $|Y|^2 \lesssim 5$ is still allowed.

In Fig. 7, we show the contour plots of \sqrt{q} in the C_1 vs. m plane with $C_2 = 1$ (left) and those in the C_2 vs. m plane with $C_1 = 1$ (right). The star marker in each panel shows the true values of parameters $(C_1, m) = (1, 1.1 \text{ TeV})$ (left) and $(C_2, m) = (1, 1.1 \text{ TeV})$ (right).

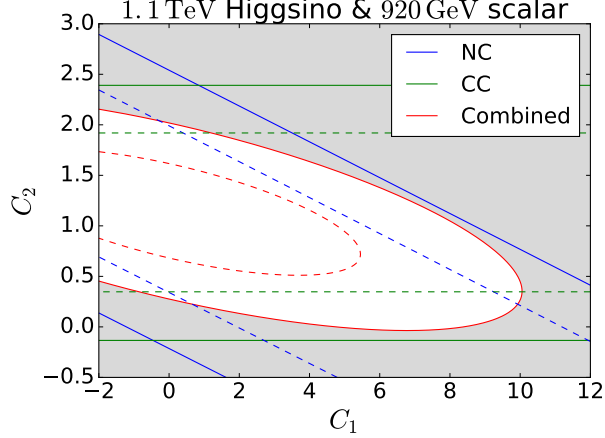


Figure 8: Contour of \sqrt{q} in the C_1 vs. C_2 plane for the 1.1 TeV Higgsino signal, tested with the scalar EWIMP assumption. The plane is defined as the scalar mass of 920 GeV. The colors and styles of lines and the meaning of the gray region are the same as Fig. 6.

Again, by combining the NC and CC results, we can significantly improve the determination of EWIMP properties, making 1σ and 2σ contours closed circles in the planes of our concern. In particular, as red lines show, the combined analysis allows us to determine the observed EWIMP mass at the level of $\mathcal{O}(10)\%$.

Finally, we comment on the possibility of discriminating between fermionic and scalar EWIMPs, whose difference comes from the loop function $f(x)$ (see Eq. (3.2)). Here we repeat the same analysis explained above, assuming the 1.1 TeV Higgsino signal for example, but use the scalar loop function to evaluate the theoretical predictions $\mathbf{x}_f(m, C_1, C_2)$. In Figs. 8 and 9, we show the results in the C_1 vs. C_2 plane and the C_1 (or C_2) vs. m plane, respectively, where one of the three parameters is fixed to its best fit value. It is seen that, in the case of the 1.1 TeV Higgsino signal, it is hard to distinguish between the bosonic and fermionic EWIMPs only with our method. However, if a part of the EWIMP properties (in particular its mass) is determined from another approach, our method may allow us to determine its spin correctly.

We also stress here that, with some favorable assumption about the observed signal, we may obtain some hint about its spin. For example, if we assume that the observed signal composes a fraction of the dark matter in our Universe, the choice of the EWIMP charges is significantly constrained. Note from Fig. 8 that the only choices of EWIMP charges that allow the EWIMP multiplet to contain an electrically neutral component are $(n, |Y|) = (3, 0), (3, 1), (4, 1/2), (4, 3/2)$, and $(5, 0)_{\text{real}}$. The last column of the table 6 shows proper choices of EWIMP masses in order for their thermal relic abundances become comparable with the dark matter abundance in the current Universe. All of those values are somewhat

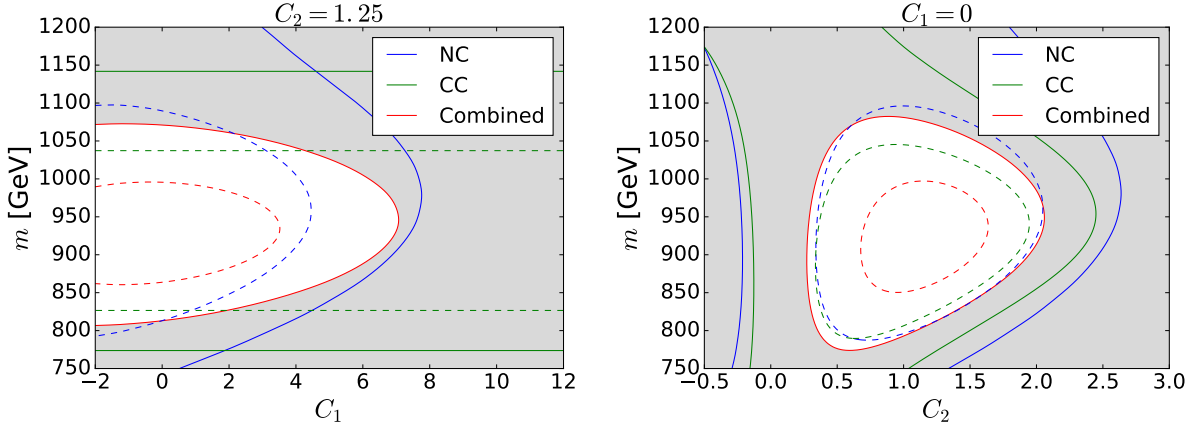


Figure 9: **Left:** Contour of \sqrt{q} in the C_1 vs. m plane with $C_2 = 1.25$ for the 1.1 TeV Higgsino signal, tested with the scalar EWIMP assumption. The colors and styles of lines and the meaning of the gray region are the same as Fig. 6. **Right:** Contour of \sqrt{q} in the C_2 vs. m plane with $C_1 = 0$ for the 1.1 TeV Higgsino signal, tested with the scalar EWIMP assumption.

| (n, Y) | C_1 | C_2 | $m_{\text{DM}}[\text{TeV}]$ |
|------------------------|-------|-------|-----------------------------|
| $(3, 0)_{\text{real}}$ | 0 | 0.25 | 2.5 [12] |
| $(3, 0)$ | 0 | 0.5 | 1.55 [35] |
| $(3, 1)$ | 0.75 | 0.5 | 1.6 [12] |
| $(4, \frac{1}{2})$ | 0.25 | 1.25 | 2.4 [12] |
| $(4, \frac{3}{2})$ | 2.25 | 1.25 | 2.9 [12] |
| $(5, 0)_{\text{real}}$ | 0 | 1.25 | 9.4 [12] |

Table 6: The scalar EWIMPs that are compatible with the result in Fig. 8. The observed DM energy density is explained by the thermal relic of the EWIMP with m_{DM} shown in the fourth column.

larger than the central value of the mass of the observed signal, which means that the scalar interpretation of the signal cannot explain the whole of the dark matter relic abundance without introducing some non-thermal production mechanism.

3.3 Conclusion

In this paper, we have discussed the indirect search of EWIMPs at future 100 TeV hadron colliders based on the precision measurement of the production processes of a charged lepton

pair and that of a charged lepton and a neutrino. In particular, we have demonstrated that not only we can discover the EWIMPs, but also we can determine their properties such as their masses, $SU(2)_L$ and $U(1)_Y$ charges, and spins via the processes of our concern. It is based on two facts: the high energy lepton production channel enables us to study its momentum distribution in great detail, and the EWIMP correction shows characteristic features, including a dip-like structure as the final state invariant mass being twice the EWIMP mass. The latter feature also helps us to distinguish the EWIMP signals from backgrounds and systematic errors, as they are not expected to show a dip-like structure. In order to fully exploit the differences between the distributions the EWIMP signals and systematic errors, we have adopted the fitting based analysis as our statistical treatment.

First, we have shown in Fig. 4 the detection reach of Higgsino and Wino from the neutral current (NC) processes (mediated by photon or Z -boson), the charged current (CC) processes (mediated by W -boson), and the combination of these two results. We have seen that the addition of the CC processes improves the detection reach from the previous analysis [36]. From the combined analysis, the bounds at the 5σ (95% C.L.) level for Higgsino and Wino are 850 GeV (1.7 TeV) and 1.3 TeV (2.3 TeV), respectively. This result, in particular that for short lifetime Higgsino, indicates the importance of our method for the EWIMP search.

Next, we have considered the determination of the mass and $SU(2)_L$ and $U(1)_Y$ charges of the observed EWIMP. By combining the NC and the CC events, the position and the height of the dip in the EWIMP effect on the cross section gives us enough information for determining all the three parameters. In Figs. 6 and 7, we have shown the plots of the test statistics that test the validity of several choices of parameters. As a result, the $SU(2)_L$ charge of the observed signal is correctly identified under the assumption of a single EWIMP multiplet, and the $U(1)_Y$ charge and mass are also determined precisely. In order for the determination of the EWIMP spin, we have plotted the contours of the test statistics that test the validity of the scalar EWIMP models with some fixed values of masses and charges. The results are shown in Figs. 8 and 9, which reveals that the spin is not completely determined by solely using our method. Use of another approach to determine the EWIMP properties, or of some assumption like that the observed signal corresponds to the dark matter in our Universe, may help us to obtain further information regarding the EWIMP spin.

Section A

Review of supersymmetry

In this appendix, we briefly review the $\mathcal{N} = 1$ supersymmetry, which is an essential element of the MSSM reviewed in Sec. 2.2. Our argument is based on [18, 37].

The $\mathcal{N} = 1$ supersymmetry is

First example is the MSSM, extension of the SM with the so-called $\mathcal{N} = 1$ supersymmetry (SUSY) [18, 37] that relates a bosonic particle and a fermionic particle. The supersymmetry transformations for a complex scalar ϕ and its “superpartner” Weyl fermion ψ are defined as

$$\delta\phi = (\epsilon\psi), \quad \delta\phi^* = (\epsilon^\dagger\psi^\dagger), \quad (\text{A.1})$$

$$\delta\psi = -i(\sigma^\mu\epsilon^\dagger)\partial_\mu\phi, \quad \delta\psi^\dagger = i(\epsilon\sigma^\mu)\partial_\mu\phi^*, \quad (\text{A.2})$$

where $\sigma^\mu \equiv (\mathbf{1}, \boldsymbol{\sigma})$ with $\boldsymbol{\sigma}$ being Pauli matrices, while ϵ is an anti-commuting Weyl fermionic object that parameterizes the SUSY transformation. The summation over the spinor indices is assumed inside each parenthesis. These transformations, if denoted by operators ϵQ and $\epsilon^\dagger Q^\dagger$, are known to form a closed algebra

$$[Q, Q^\dagger] = 2i\sigma^\mu\partial_\mu, \quad (\text{A.3})$$

$$[Q, Q] = [Q^\dagger, Q^\dagger] = 0, \quad (\text{A.4})$$

when fields are on-shell.^{‡13}

^{‡13}In order for the algebra to be closed off-shell, one can introduce a new scalar field F without a kinetic term that is often called as an *auxiliary* field. F works as a Lagrange multiplier whose equation of motion

References

- [1] F. Zwicky, Die Rotverschiebung von extragalaktischen Nebeln, *Helvetica Physica Acta* 6 (1933) 110.
- [2] F. Zwicky, On the Masses of Nebulae and of Clusters of Nebulae, *Astrophysical Journal* 86 (1937) 217.
- [3] V. Trimble, Existence and Nature of Dark Matter in the Universe, *Ann. Rev. Astron. Astrophys.* 25 (1987) 425–472. [doi:10.1146/annurev.aa.25.090187.002233](#).
- [4] H. W. Babcock, The rotation of the Andromeda Nebula, *Lick Observatory Bulletin* 19 (1939) 41–51. [doi:10.5479/ADS/bib/1939LicOB.19.41B](#).
- [5] K. G. Begeman, A. H. Broeils, R. H. Sanders, Extended rotation curves of spiral galaxies: Dark haloes and modified dynamics, *Mon. Not. Roy. Astron. Soc.* 249 (1991) 523.
- [6] G. Jungman, M. Kamionkowski, A. Kosowsky, D. N. Spergel, Weighing the universe with the cosmic microwave background, *Phys. Rev. Lett.* 76 (1996) 1007–1010. [arXiv:astro-ph/9507080](#), [doi:10.1103/PhysRevLett.76.1007](#).
- [7] G. Jungman, M. Kamionkowski, A. Kosowsky, D. N. Spergel, Cosmological parameter determination with microwave background maps, *Phys. Rev. D* 54 (1996) 1332–1344. [arXiv:astro-ph/9512139](#), [doi:10.1103/PhysRevD.54.1332](#).
- [8] N. Aghanim, et al., Planck 2018 results. VI. Cosmological parameters (2018). [arXiv:1807.06209](#).
- [9] P. Gondolo, G. Gelmini, Cosmic abundances of stable particles: Improved analysis, *Nucl. Phys. B* 360 (1991) 145–179. [doi:10.1016/0550-3213\(91\)90438-4](#).
- [10] G. Belanger, F. Boudjema, A. Pukhov, A. Semenov, MicrOMEGAs: A Program for calculating the relic density in the MSSM, *Comput. Phys. Commun.* 149 (2002) 103–120. [arXiv:hep-ph/0112278](#), [doi:10.1016/S0010-4655\(02\)00596-9](#).
- [11] G. Bélanger, F. Boudjema, A. Goudelis, A. Pukhov, B. Zaldivar, micrOMEGAs5.0 : Freeze-in, *Comput. Phys. Commun.* 231 (2018) 173–186. [arXiv:1801.03509](#), [doi:10.1016/j.cpc.2018.04.027](#).
- [12] M. Farina, D. Pappadopulo, A. Strumia, A modified naturalness principle and its experimental tests, *JHEP* 08 (2013) 022. [arXiv:1303.7244](#), [doi:10.1007/JHEP08\(2013\)022](#).

-
- [13] N. Arkani-Hamed, A. Delgado, G. F. Giudice, The Well-tempered neutralino, Nucl. Phys. B741 (2006) 108–130. [arXiv:hep-ph/0601041](#), [doi:10.1016/j.nuclphysb.2006.02.010](#).
- [14] J. Hisano, S. Matsumoto, M. Nagai, O. Saito, M. Senami, Non-perturbative effect on thermal relic abundance of dark matter, Phys. Lett. B646 (2007) 34–38. [arXiv:hep-ph/0610249](#), [doi:10.1016/j.physletb.2007.01.012](#).
- [15] M. Cirelli, A. Strumia, M. Tamburini, Cosmology and Astrophysics of Minimal Dark Matter, Nucl. Phys. B787 (2007) 152–175. [arXiv:0706.4071](#), [doi:10.1016/j.nuclphysb.2007.07.023](#).
- [16] T. Moroi, M. Nagai, M. Takimoto, Non-Thermal Production of Wino Dark Matter via the Decay of Long-Lived Particles, JHEP 07 (2013) 066. [arXiv:1303.0948](#), [doi:10.1007/JHEP07\(2013\)066](#).
- [17] M. Beneke, A. Bharucha, F. Dighera, C. Hellmann, A. Hryczuk, S. Recksiegel, P. Ruiz-Femenia, Relic density of wino-like dark matter in the MSSM, JHEP 03 (2016) 119. [arXiv:1601.04718](#), [doi:10.1007/JHEP03\(2016\)119](#).
- [18] S. P. Martin, A Supersymmetry primer (1997) 1–98[Adv. Ser. Direct. High Energy Phys.18,1(1998)]. [arXiv:hep-ph/9709356](#), [doi:10.1142/9789812839657_0001](#), [10.1142/9789814307505_0001](#).
- [19] M. Cirelli, N. Fornengo, A. Strumia, Minimal dark matter, Nucl. Phys. B753 (2006) 178–194. [arXiv:hep-ph/0512090](#), [doi:10.1016/j.nuclphysb.2006.07.012](#).
- [20] M. Cirelli, A. Strumia, Minimal Dark Matter: Model and results, New J. Phys. 11 (2009) 105005. [arXiv:0903.3381](#), [doi:10.1088/1367-2630/11/10/105005](#).
- [21] J. Hisano, S. Matsumoto, M. M. Nojiri, O. Saito, Non-perturbative effect on dark matter annihilation and gamma ray signature from galactic center, Phys. Rev. D71 (2005) 063528. [arXiv:hep-ph/0412403](#), [doi:10.1103/PhysRevD.71.063528](#).
- [22] J. Alwall, M. Herquet, F. Maltoni, O. Mattelaer, T. Stelzer, MadGraph 5 : Going Beyond, JHEP 06 (2011) 128. [arXiv:1106.0522](#), [doi:10.1007/JHEP06\(2011\)128](#).
- [23] J. Alwall, R. Frederix, S. Frixione, V. Hirschi, F. Maltoni, O. Mattelaer, H. S. Shao, T. Stelzer, P. Torrielli, M. Zaro, The automated computation of tree-level and next-to-leading order differential cross sections, and their matching to parton shower simulations, JHEP 07 (2014) 079. [arXiv:1405.0301](#), [doi:10.1007/JHEP07\(2014\)079](#).

-
- [24] T. Sjöstrand, S. Ask, J. R. Christiansen, R. Corke, N. Desai, P. Ilten, S. Mrenna, S. Prestel, C. O. Rasmussen, P. Z. Skands, An Introduction to PYTHIA 8.2, Comput. Phys. Commun. 191 (2015) 159–177. [arXiv:1410.3012](#), [doi:10.1016/j.cpc.2015.01.024](#).
- [25] J. de Favereau, C. Delaere, P. Demin, A. Giammanco, V. Lemaître, A. Mertens, M. Selvaggi, DELPHES 3, A modular framework for fast simulation of a generic collider experiment, JHEP 02 (2014) 057. [arXiv:1307.6346](#), [doi:10.1007/JHEP02\(2014\)057](#).
- [26] R. D. Ball, V. Bertone, S. Carrazza, L. Del Debbio, S. Forte, A. Guffanti, N. P. Hartland, J. Rojo, Parton distributions with QED corrections, Nucl. Phys. B877 (2013) 290–320. [arXiv:1308.0598](#), [doi:10.1016/j.nuclphysb.2013.10.010](#).
- [27] M. Aaboud, et al., Search for a new heavy gauge boson resonance decaying into a lepton and missing transverse momentum in 36 fb^{-1} of pp collisions at $\sqrt{s} = 13 \text{ TeV}$ with the ATLAS experiment, Eur. Phys. J. C78 (5) (2018) 401. [arXiv:1706.04786](#), [doi:10.1140/epjc/s10052-018-5877-y](#).
- [28] A. M. Sirunyan, et al., Search for high-mass resonances in final states with a lepton and missing transverse momentum at $\sqrt{s} = 13 \text{ TeV}$, JHEP 06 (2018) 128. [arXiv:1803.11133](#), [doi:10.1007/JHEP06\(2018\)128](#).
- [29] T. Aaltonen, et al., Search for new particles decaying into dijets in proton-antiproton collisions at $\sqrt{s} = 1.96 \text{ TeV}$, Phys. Rev. D79 (2009) 112002. [arXiv:0812.4036](#), [doi:10.1103/PhysRevD.79.112002](#).
- [30] G. Cowan, K. Cranmer, E. Gross, O. Vitells, Asymptotic formulae for likelihood-based tests of new physics, Eur. Phys. J. C71 (2011) 1554, [Erratum: Eur. Phys. J. C73,2501(2013)]. [arXiv:1007.1727](#), [doi:10.1140/epjc/s10052-011-1554-0](#), [doi:10.1140/epjc/s10052-013-2501-z](#).
- [31] A. Buckley, J. Ferrando, S. Lloyd, K. Nordström, B. Page, M. Rüfenacht, M. Schönherr, G. Watt, LHAPDF6: parton density access in the LHC precision era, Eur. Phys. J. C75 (2015) 132. [arXiv:1412.7420](#), [doi:10.1140/epjc/s10052-015-3318-8](#).
- [32] L. Di Luzio, R. Gröber, G. Panico, Probing new electroweak states via precision measurements at the LHC and future colliders, JHEP 01 (2019) 011. [arXiv:1810.10993](#), [doi:10.1007/JHEP01\(2019\)011](#).
- [33] S. Matsumoto, S. Shirai, M. Takeuchi, Indirect Probe of Electroweak-Interacting Particles with Mono-Lepton Signatures at Hadron Colliders (2018). [arXiv:1810.12234](#).

- [34] M. Tanabashi, et al., Review of Particle Physics, Phys. Rev. D98 (3) (2018) 030001. [doi:10.1103/PhysRevD.98.030001](#).
- [35] E. Del Nobile, M. Nardecchia, P. Panci, Millicharge or Decay: A Critical Take on Minimal Dark Matter, JCAP 1604 (04) (2016) 048. [arXiv:1512.05353](#), [doi:10.1088/1475-7516/2016/04/048](#).
- [36] S. Chigusa, Y. Ema, T. Moroi, Probing electroweakly interacting massive particles with Drell-Yan process at 100 TeV hadron colliders, Phys. Lett. B789 (2019) 106–113. [arXiv:1810.07349](#), [doi:10.1016/j.physletb.2018.12.011](#).
- [37] J. Wess, J. A. Bagger, [Supersymmetry and supergravity; 2nd ed.](#), Princeton Series in Physics, Princeton Univ. Press, Princeton, NJ, 1992.
URL <https://cds.cern.ch/record/320631>